Establishing Upper Limits on Neuronal Activity–Evoked pH Changes With APT-CEST MRI at 7 T

Vitaliy Khlebnikov,[1]* Jeroen C.W. Siero,[1,2] Alex A. Bhogal,[1] Peter R. Luijten,[1] Dennis W.J. Klomp,[1] and Hans Hoogduin[1]

Purpose: To detect neuronal activity–evoked pH changes by amide proton transfer–chemical exchange saturation transfer (APT-CEST) MRI at 7 T.
Methods: Three healthy subjects participated in the study. A low-power 3-dimensional APT-CEST sequence was optimized through the Bloch-McConnell equations. pH sensitivity of the sequence was estimated both in phantoms and in vivo. The feasibility of pH–functional MRI was tested in Bloch-McConnell-simulated data using the optimized sequence. In healthy subjects, the visual stimuli were used to evoke transient pH changes in the visual cortex, and a 3-dimensional APT-CEST volume was acquired at the pH-sensitive frequency offset of 3.5 ppm every 12.6 s.
Results: In theory, a three-component general linear model was capable of separating the effects of blood oxygenation level–dependent contrast and pH. The Bloch-McConnell equations indicated that a change in pH of 0.03 should be measurable at the experimentally determined temporal signal-to-noise ratio of 108. However, only a blood oxygenation level–dependent effect in the visual cortex could be discerned during the visual stimuli experiments performed in the healthy subjects.
Conclusions: The results of this study suggest that if indeed there are any transient brain pH changes in response to visual stimuli, those are under 0.03 units pH change, which is extremely difficult to detect using the existent techniques.
Magn Reson Med 80:126–136, 2018. © 2017 The Authors Magnetic Resonance in Medicine published by Wiley Periodicals, Inc. on behalf of International Society for Magnetic Resonance in Medicine. This is an open access article under the terms of the Creative Commons Attribution NonCommercial License, which permits use, distribution and reproduction in any medium, provided the original work is properly cited and is not used for commercial purposes.

INTRODUCTION

Traditional methods of mapping brain neuronal activity rely on blood oxygenation level–dependent (BOLD) contrast. Blood oxygenation level–dependent contrast is sensitive to T_2^* contrast and originates from the inhomogeneity in the magnetic field as a result of variation in blood oxygen level, cerebral blood flow, and cerebral blood volume (1–3). A whole cascade of physiological processes take place between brain neuronal activity and changes in the hemodynamic properties of the surrounding vasculature, measured by BOLD functional MRI (fMRI). The BOLD-fMRI measures neuronal activity indirectly; therefore, it suffers from the low specificity, as the mechanisms underlying the neurovascular coupling may be altered (such as in pathology and disorder) (4,5).

Normal functioning of all cellular processes critically depends on pH homeostasis. There is a great body of literature suggesting that neuronal activity gives rise to pH shifts in both the intra- and extracellular milieu (6–9). Sustained neuronal activity triggers acidification of the cytosol through metabolic production of CO_2, lactic acid, internal H^+ ions released in response to elevated Ca^{2+} levels, and acid influx through ligand- or voltage-gated channels (11–14). Interestingly, neuronal behavior itself can be modulated by small shifts in intracellular pH (pHi), as pH-dependent activity of ion channels may influence neuronal excitability (15). Noninvasive means of mapping these local and global transient pHi changes present a unique way of looking at brain activation, which may shed light on the mechanisms underlying many neurological and psychological disorders. The challenge, however, is to separate the pHi effect from concurrent T_2^*-dependent BOLD effects.

A variety of methods to measure pH noninvasively are described in the literature. Phosphorous-31 (^{31}P) magnetic resonance spectroscopy (MRS) is a current gold standard (16–18). The pH calculations of ^{31}P MRS are based on changes in chemical shift between a pH-sensitive probe (i.e. inorganic phosphate (Pi) and a pH-insensitive reference, such as phosphocreatine). However, ^{31}P MRS suffers from inherently low resolution (typical acquisition volume = 3 cm isotropic), low signal-to-noise ratio, and long scan times (upwards of 5 min). Despite being highly specific to pH of the cytosol (19,20), these current limitations make it very challenging for ^{31}P MRS to map neuronal activity–elicited transient pHi changes.

[1]Department of Radiology, Image Sciences Institute, University Medical Center Utrecht, Utrecht, Netherlands.

[2]Spinoza Centre for Neuroimaging, Amsterdam, Netherlands.

*Correspondence to: Vitaliy Khlebnikov, Ph.D., University Medical Center Utrecht, Department of Radiology, Heidelberglaan 100, Q.02.4.308, Utrecht, 3584 CX, Netherlands. E-mail: v.khlebnikov@umcutrecht.nl

Other approaches used to measure pH have been based on spin locking (21) and chemical exchange saturation transfer (CEST) (22) methods, both of which probe the inherently pH-dependent chemical-exchange process between the selectively saturated labile proton pool and the abundant water proton pool. For instance, Magnotta et al. used on-resonance spin locking to measure spin-lattice relaxation time (T_1) in the rotating frame ($T_{1\rho}$) to map brain neuronal activity by measuring pH changes in the human brain elicited by the visual stimulus (23). The authors noticed a similar activation pattern between BOLD and $T_{1\rho}$, with the latter being independent of blood oxygenation. In response to the visual stimulation in the healthy subject, a change in pHi of approximately 0.1 was measured by ^{31}P MRS, so the authors concluded that the observed $T_{1\rho}$ changes were the result, at least in part, of pH, thereby presenting pH-fMRI as a new way of looking at brain activity. However, many mechanisms may contribute to $T_{1\rho}$ relaxation in biological tissue, depending on the sequence parameters (e.g., macromolecules (24), pH (25), diffusion (26–28), cerebral blood volume (29), inflow (30), BOLD (28)). In addition, on-resonance $T_{1\rho}$ does not differentiate among the different metabolites present in vivo, many of which may exhibit direct and inverse relationships of their corresponding chemical-exchange processes with pH (31). As a result, the origin of $T_{1\rho}$ contrast in vivo should be treated with caution, as the effects of BOLD and inflow can be readily mistaken for the desired pH effect.

Recently, amide proton transfer (APT) CEST, the contrast of which is believed to predominantly originate from intracellular amides (32–35), was applied to quantitative pHi mapping in hyperacute stroke patients (36). The technique showed potential in identifying the ischemic penumbra following the stroke (36–40), and a pH drop of 0.1 in the ischemic tissue was quantified (36). In addition, CEST is an image-based technique that allows for an inherently high spatial resolution. The high pHi sensitivity and specificity at high resolution turn APT-CEST into an attractive tool to study neuronal activity–elicited fast transient pHi changes in the brain.

In this work, we present our initial attempts at detecting neuronal activity–evoked pHi changes using APT-CEST at 7 T. First, we used the Block-McConnell simulations to optimize a 3-dimensional (3D) steady-state, low-power, pulsed APT-CEST sequence in terms of sequence timing and sensitivity to the pH-dependent APT-CEST effect with the subsequent pH-sensitivity estimations in phantoms. Second, we manipulated arterial carbon dioxide level in the healthy human subjects to modulate brain pHi and estimated ΔpHi limit of detection for the optimized APT-CEST sequence in vivo. Then, a three-component general linear model was designed to separate BOLD and pHi effects in the Block-McConnell simulated data. Finally, the model, tested in the simulations, was applied to the in vivo experiments to separate BOLD and pHi effects evoked by the visual stimulus during the flashing checkboard in the healthy human subjects.

THEORY

The chemical-exchange contrast depends on a number of parameters including the rate of chemical exchange between the labile metabolite protons and the abundant exchange-mediating water proton pool (k_{ex}) and the Larmor frequency separation between them ($\Delta\omega$). In a CEST experiment, a so-called Z-spectrum is acquired (22), which is a plot of the normalized attenuated water-signal intensity versus off-resonance saturation frequency ($\Delta\omega$.). The water is assigned a chemical shift of 0 ($\Delta\omega = 0$, i.e., on resonance), and the labile protons of the endogenous metabolites contribute to the water-signal attenuation downfield ($\Delta\omega$ in the range of 0–5 ppm) from the water resonance. Most of those labile protons have distinct off-resonance frequencies, such as hydroxyl protons (0–1.5 ppm), amino protons (1.8–3 ppm), and amide protons (3.3–3.8 ppm). The CEST effect for each type of labile proton depends on the metabolite concentration and pH-dependent exchange rate (k_{ex}). The exchange rate of amide protons is base-catalyzed in the physiological pH range (i.e., it depends on the hydroxyl ions concentration), and therefore reflects changes in pH. This specificity, present in CEST but absent in on-resonance spin locking, allows the labile protons of a certain type to be probed independently of the others, making CEST contrast more pH-specific.

METHODS

Numerical Simulations: Sequence Optimization

A 3D steady-state pulsed CEST sequence (41) was optimized for maximum sensitivity to APT-CEST effect through the Bloch-McConnell equation simulations (42). The following sequence parameters were investigated: the number of saturation pulses (saturation time), transmit field amplitude of CEST saturation prepulse (B_1 is used as the peak amplitude throughout the paper), and radiofrequency (RF) duty cycle. All other sequence parameters are the same as for data acquisition (see subsequently).

Four-pool (free water in tissue, APT-CEST, nuclear Overhauser Enhancement and magnetization transfer) Bloch-McConnell equations were solved numerically (43), assuming the following gray-matter pool parameters: free-water pool ($T_1/T_2 = 1.9$ s/55 ms), APT pool ($T_2 = 10$ ms, $\Delta\omega = 3.5$ ppm, $M_0 = 0.13\%$, R = 22.2 Hz), nuclear Overhauser Enhancement pool ($T_2 = 0.3$ ms, $\Delta\omega = -3.5$ ppm, $M_0 = 3\%$, R = 10 Hz), and magnetization-transfer pool ($T_2 = 10\,\mu s$, $\Delta\omega = -2.4$ ppm, $M_0 = 3\%$, R = 50 Hz) (44). The T_1 values of other than water pools (i.e., APT-CEST, nuclear Overhauser Enhancement, and magnetization transfer) were fixed to 1 s (45).

An assumption was made that there are only four pools in the system and that the only interactions are with water. The APT-CEST effect size (contribution to the z-spectrum) was quantified by the pool difference method as follows:

$$Amide\text{-}CEST = Mz(3.5ppm, M_A = 0) \atop /M0 - Mz(3.5ppm, M_A = 1)/M0 \qquad [1]$$

where APT-CEST is the effect size of cytosolic amides, $M_z(\Delta\omega, M_A)$ is the signal in the z-spectrum at $\Delta\omega$, M_0 is the steady-state signal at 300 ppm, and M_A is the amplitude of the APT-CEST compartment ($M_A = 0$ and $M_A = 1$

(i.e., without and with APT pool, respectively)). A Gaussian noise of 1% (of the steady-state signal at 300 ppm) was added to the simulated data.

Numerical Simulations: fMRI Data and Separation of BOLD and pHi Effects

The pHi-fMRI data were simulated using four-pool Bloch-McConnell equations (42,43) by changing an exchange rate (k_{ex}) of APT-CEST pool (from 22.2 Hz at pH = 7.0 to 17.6 Hz at pH = 6.9, using the following relationship: $pHi = \log_{10}k_{ex} + 5.654$ derived in (35)) during the visual stimulation, and assuming a BOLD signal change of 1.1% (APT-CEST signal change at 3.5 ppm due to BOLD effect) and a ΔpHi of 0.1 (or 0.52% APT-CEST signal change at 3.5 ppm due to pH effect). A BOLD effect of 1.1% was assumed based on a short echo time of the CEST sequence used, whereas a ΔpHi of approximately 0.1 was previously measured by ^{31}P MRS (23) during the visual stimulation. Because the only varied CEST parameter was pHi, APT-CEST signal change reflects ΔpHi. A Gaussian noise of 1.5% (of the steady-state signal at 300 ppm) was added to the simulated data for a final temporal SNR of 108, to match that of the experimental data.

To separate the pHi effect from BOLD signal changes, a general linear model was composed of three regressors: (i) BOLD, (ii) pHi, and (iii) APT-CEST signal (M_z (3.5 ppm)) variation, as a result of switching the RF CEST prepulse "on" and "off." The BOLD effect was assumed to be activated when visual stimulus was "on" (regardless of RF CEST prepulse being "on" or "off"). The pHi effect was assumed to be activated when both the visual stimulus and RF CEST prepulse were "on." A visual explanation of the three-regressor model is provided in the "Results" section. All other sequence parameters and the fMRI paradigm are the same as for data acquisition (see subsequently).

Data Acquisition

This study was approved by the Medical Research Ethics Committee of University Medical Center Utrecht, and all of the volunteers gave informed consent. All experiments were done according to the guidelines and regulations of the Wet Medisch Wetenschappelijk Onderzoek. Three subjects were scanned on a 7T Achieva MR system (Philips, Best, Netherlands) using a quadrature transmit coil with a 32-channel receive head coil (NOVA Medical, Houston, Texas, USA).

Three-Dimensional Steady-State CEST Protocol

A 3D steady-state pulsed CEST sequence at 7 T was first introduced in (41) because of its power efficiency, low specific absorption rate, and low system burden compared with continuous-saturation CEST schemes. The steady-state sequence consists of a short RF pulse for presaturation (applied at the off-resonance frequency of the metabolite of interest), a gradient spoiler to destroy the residual magnetization in the x-y plane, and a segmented echo-planar-imaging readout. All of these components add up to a relatively short repetition time, which is repeated multiple times to reach the steady

state. During the steady-state signal build-up, the k-space is acquired from the edge to the center of the k-space center, and the k-space center is sampled after the steady state has been achieved. The temporal resolution of a steady-state sequence is limited by the amount of time it takes to reach the steady state.

In this work, a low-power 3D steady-state CEST sequence was used with the following scan parameters: 1.5-µT (peak amplitude) saturation prepulse (a single RF-spoiled 8-ms (267-Hz bandwidth) sinc-Gaussian pulse followed by a 50-mT/m spoiler of 10 ms) interleaved with a sagittal, segmented echo-planar imaging readout (echo-planar imaging factor 7 with a binomial RF pulse for water-only excitation, repetition time/echo time/flip angle = 25 ms/4.2 ms/12°, field of view = 150 × 225 × 190, matrix size 128), voxel size = 2 mm isotropic, sensitivity-encoding factor 1.9 (anterior–posterior) and 2.4 (right–left), center of k-space weighted acquisition with the k-space center measured at 6.9 s, time per volume = 12.6 s. The data were acquired at two frequencies, 3.5 and 300 ppm, for the breathing experiments, and at 3.5 ppm (alternating saturation RF CEST prepulse between "on" and "off") for the pHi-fMRI experiments. Both alternating schemes (3.5 versus 300 ppm and RF CEST prepulse "on" versus "off") were used to determine the remaining BOLD effect in the data. The data at 300 ppm and with RF switched "off" serve the same purpose and can be acquired interchangeably. For fMRI experiments, however, data acquisition with RF CEST prepulse switched "off" (instead of data at 300 ppm) is preferred, because of the RF amplifiers' duty cycle limitations. A T_1-weighted anatomical scan was used to create masks of white matter and gray matter, which were subsequently used to calculate white-matter and gray-matter averaged CEST signals. Third-order shims were applied to improve the homogeneity of the magnetic field across the whole brain.

Demonstration of pH Sensitivity

To validate the sensitivity of the sequence to changes in pH, dual phantoms were created with 10% (wt/vol) bovine serum albumin (BSA, ~66 kD) and 10 mM phosphocreatine in 10-mM phosphate-buffered solution as a pH buffering system containing 0.1% sodium azide for phantom preservation. Overall, six phantoms were made in 50-mL Falcon centrifuge tubes (Fisher Scientific, Hampton, New Hampshire, USA), and pH was adjusted to 5.5, 6.0, 6.5, 7.0, 7.5, and 8.0 by NaOH and HCl. All chemicals were purchased from Sigma-Aldrich (Zwijndrecht, Netherlands) and used as received without further purification. The phantom measurements were performed at room temperature.

Carbon-Dioxide Breathing Experiments

The CO_2 breathing experiments were done to estimate the ΔpHi detection limit of the optimized CEST sequence. The brain pHi was modulated by carbon dioxide delivered using a computer-controlled gas delivery system (RespirAct, Thornhill Research Inc, Toronto, Ontario, Canada). During the breathing experiments, the volunteers were scanned throughout a hypercapnic breathing challenge (6 min) in which end-tidal CO_2
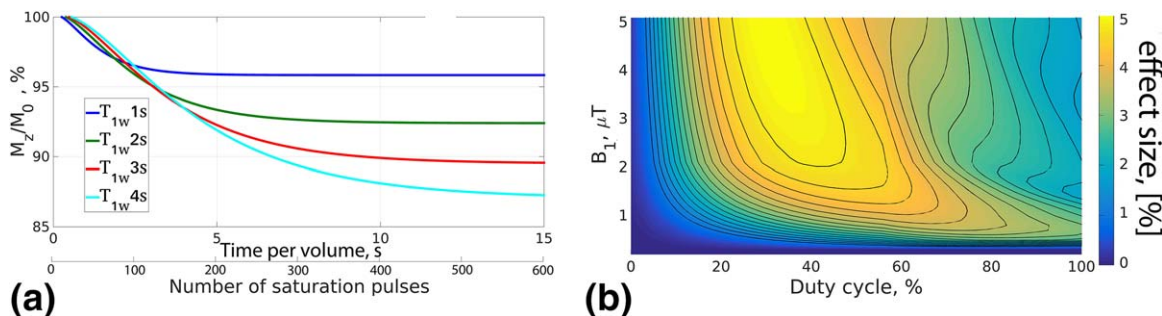
FIG. 1. **a**: The Bloch-McConnell equations were used to simulate the approach to the steady state (M_z/M_o, %) at a B_1 of 1.5 μT (peak amplitude) versus the number of saturation pulses (also recalculated as time-per-volume on the second axis) as a function of various water-T_1 relaxation times. **b**: The simulated 3-dimensional plots of amide proton transfer–chemical exchange saturation transfer (APT-CEST) effect size as a function of B_1 amplitude and duty cycle. The contour lines overlaid are meant to delineate the regions of the same APT-CEST effect size. The frequency offsets used for (**a**) and (**b**) are that of amide protons (3.5 ppm).

($PetCO_2$) was targeted at 10 mmHg above individual subject baseline levels. CO_2 was used as a stimulus to change the brain pHi (24). These changes were then investigated using APT-CEST MRI and ^{31}P MRS.

^{31}P MRS Protocol

For quantitative pHi measurements, 3D ^{31}P chemical shift imaging (echo time/repetition time = 0.5 ms/250 ms, field of view = $480 \times 180 \times 320\,mm^3$, resolution = $20 \times 20 \times 20\,mm^3$ isotropic, 2 min 25 s per scan, $N=2$) was performed using inorganic phosphate and phosphocreatine as a probe and a reference, respectively (46).

Functional MRI Protocol

Functional imaging was performed using the APT-CEST sequence. The visual paradigm consisted of 10 blocks. Four equal-duration cycles of flashing checkerboard were interleaved with a 126-s period of visual fixation, followed by two extra cycles of visual fixation. A total of 100 3D volumes were acquired at the off-resonance frequency offset of 3.5 ppm (pH sensitive APT-CEST effect) by alternating RF CEST prepulse "on" (with CEST prepulse) and "off" (no CEST prepulse). The APT-CEST signal (M_z (3.5 ppm)) variation due to the RF CEST prepulse switching was used

as a third regressor, in addition to the regressors describing the time variation of BOLD and pHi. The total acquisition time was 21 min 14 s.

The stimulus was an 8-Hz flickering black and white checkerboard with a red fixating dot in the middle. The rest condition was a uniform gray stimulus with the same red fixating dot in the middle. The subjects participating in the fMRI experiments were experienced volunteers. After the experiments, confirmation was obtained from all subjects that the subjects were on task.

Data Processing

A general linear model (FSL, fMRI Expert Analysis Tool) consisting of three regressors (BOLD, pHi, and APT-CEST signal (M_z (3.5 ppm)) variation as a result of RF CEST prepulse switching "on" and "off" was used to generate individual statistical maps and to calculate signal change. The last regressor was used to separate the effects of BOLD and pHi. Coregistration and segmentation were done in FSL (FMRIB version 6.0, FLIRT, Oxford, United Kingdom) (47,48). To compensate for B_0 inhomogeneity, whole-brain white-matter and gray-matter masks were further intersected by the corresponding B_0 maps thresholded in between ±0.1 ppm.
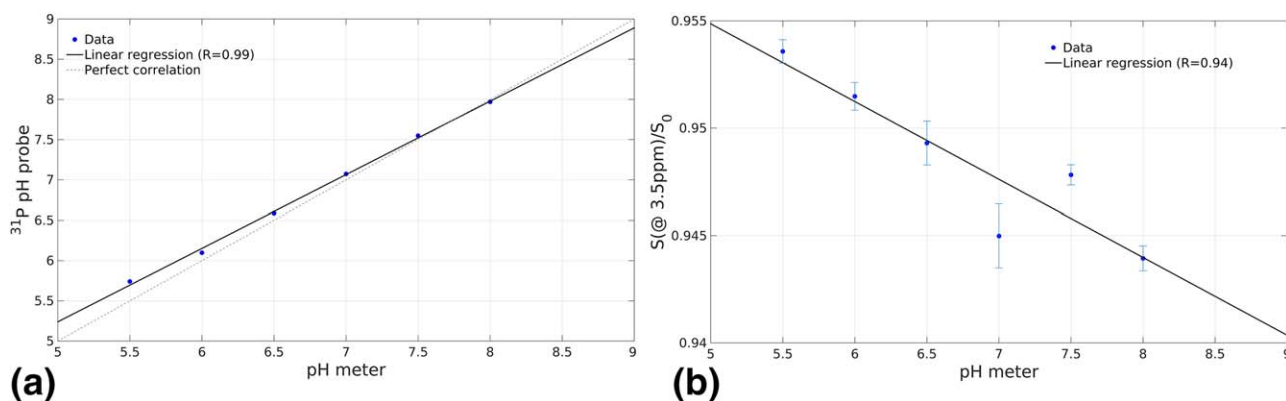

FIG. 2. **a**: Plot of ^{31}P magnetic resonance spectroscopy–calculated pH values versus pH-meter-based measurements in dual bovine serum albumin/phosphocreatine phantoms. **b**: The plot of S(@3.5ppm)/S_0 versus pH-meter-based measurements are for the same phantoms. Black lines represent the linear regression analysis.
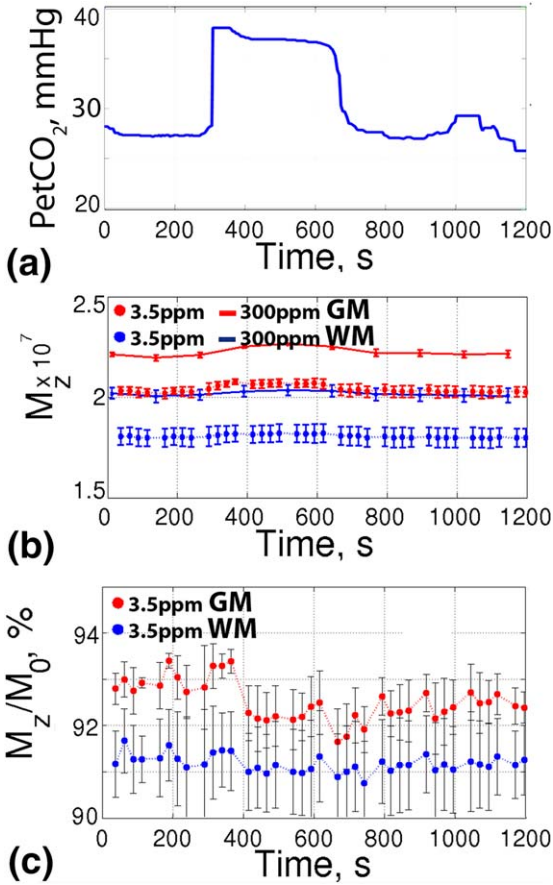
FIG. 3. **a**: The breathing paradigm depicting the end-tidal CO_2 (PetCO$_2$) trace measured by the RespirAct. **b**: Densely sampled dynamic APT-CEST (at 3.5 ppm) and off-resonance control (at 300 ppm) points ($N = 3$) in response to (**a**). **c**: Same as (**b**), only APT-CEST signals are normalized point-wise by the fitted control points. The data in (**b**) and (**c**) are whole-brain averaged for white matter (WM) and gray matter (GM).

Temporal SNR in the visual cortex was calculated as

$$tSNR = \frac{S}{SD} \qquad [2]$$

where S and SD are the mean signal and the standard deviation, respectively, in the visual cortex across 30 dynamic images acquired at 3.5 ppm without visual stimulation.

Simulations and further image processing and analysis were done using MATLAB (The MathWorks Inc, Natick, Massachusetts, USA).

RESULTS

In Figure 1, using the Bloch-McConnell simulations, the CEST sequence was optimized in terms of the temporal resolution (Fig. 1a), and the sensitivity to APT-CEST effect (Fig. 1b). Figure 1a shows the APT-CEST signal (M_z/M_o, %) during the approach to the steady state as a function of the number of saturation pulses (or repetition-time repeats), for various water T_1 (T_{1w}) relaxation times. The signal scales with T_{1w} also govern the
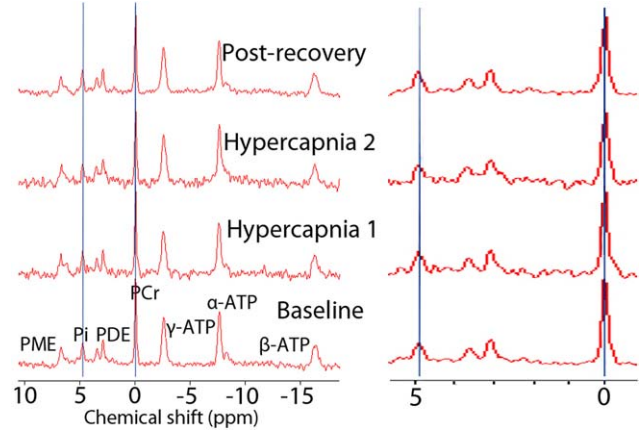
FIG. 4. Representative single-voxel gray-matter ^{31}P spectrum averaged across three healthy subjects. The spectra shown correspond to four consecutive time points in the experiments: (1) baseline or normal breathing; (2) first hypercapnic challenge (+10 mmHg CO_2, same breathing paradigm as in Fig. 3a); (3) second hypercapnic challenge (+10 mmHg CO_2, same breathing paradigm as in Fig. 3a) performed 5 min after the first one; and (4) 10-min postrecovery normal breathing. Adenosine triphosphate (ATP), phosphocreatine (PCr), phosphodiesters (PDE), inorganic phosphate (Pi), and phosphomonoesters (PME). The black vertical lines show the positions of Pi and PCr with respect to the baseline. The inset shows a zoomed-in image in the region 0 to 5 ppm across all spectra.

rate at which the steady state is achieved. The longer the T_{1w}, the more saturation pulses are required to reach the steady state, and hence the lower the temporal resolution. Assuming a maximum tissue T_{1w} of 2.5 s (49,50) for a normal brain, the steady state (signal change within 0.5%) is reached in 6.9 s. This translates to 504 saturation pulse, which corresponds to the temporal resolution of 12.6 s.

The optimum saturation time parameters determined in Figure 1a were used to find the optimum saturation pulse (B_1 amplitude and duty cycle) parameters in Figure 1b. Both B_1 amplitude and duty cycle were varied to cover all possible ranges, and their influence on APT-CEST effect size is depicted. Taking into account RF
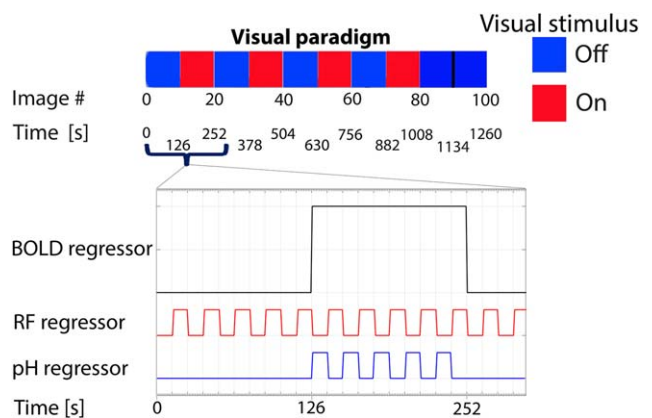

FIG. 5. Functional MRI (fMRI) visual stimulus paradigm with a schematic of the three-regressor model fitted to both simulated and experimental data.
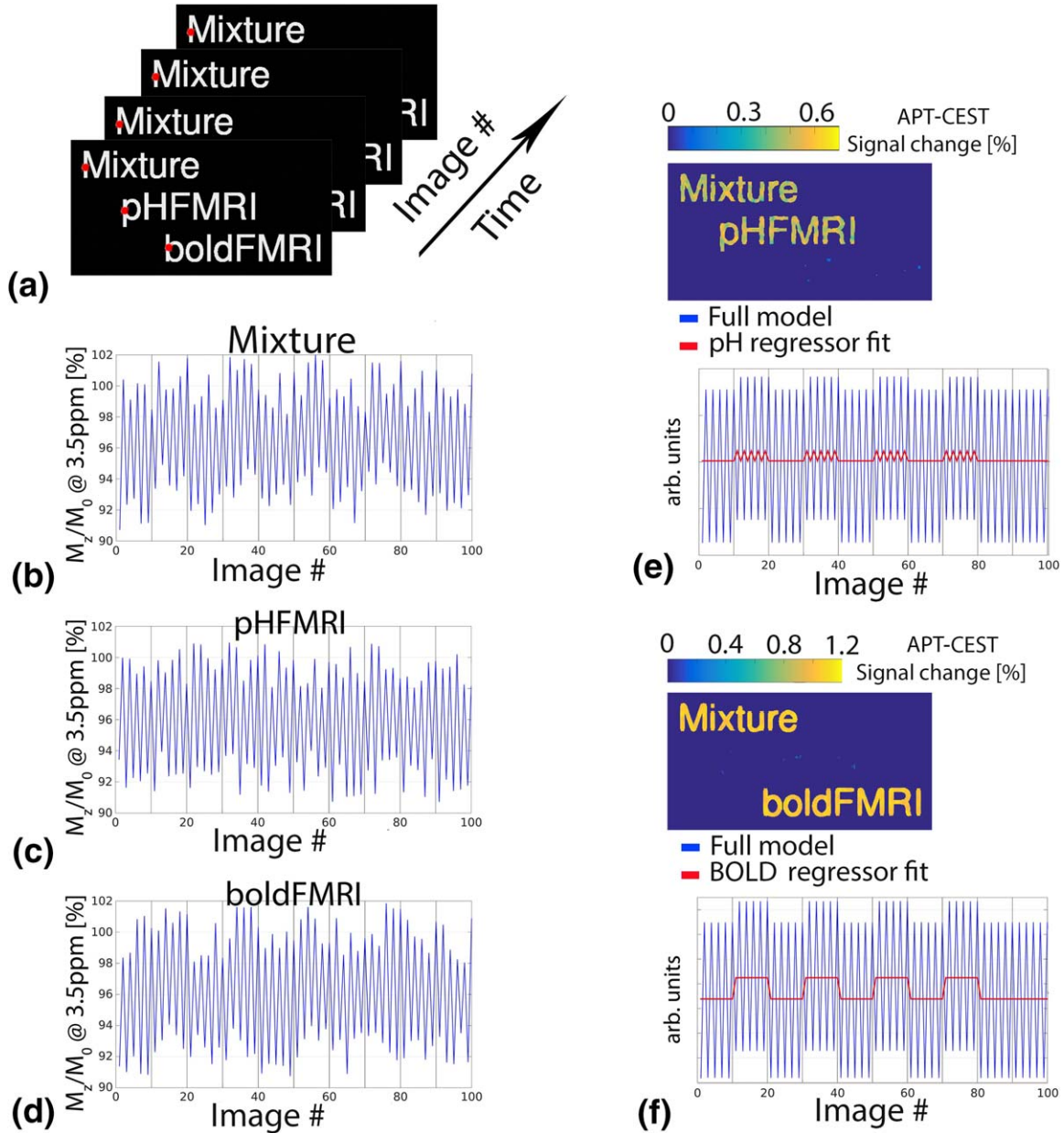
FIG. 6. The Bloch-McConnell simulated data. **a**: A time series of 2-dimensional fMRI dynamic images 3-dimensional stack matrix size of 260 × 500 × 100), corresponding to the visual paradigm in Figure 5, with the three simulated time-dependent effects: (i) a combination of blood oxygen–level dependent (BOLD) (1.1%) and intracellular pH (pHi) (ΔpHi of 0.1 or 0.52% APT-CEST signal change at 3.5 ppm) encoded in the "Mixture" region of interest (ROI) (first row, its time series in (**b**)); (ii) a control for only pHi encoded in the "pHFMRI" ROI (second row, its time series in (**c**)); and (iii) a control for only BOLD encoded in the "boldFMRI" (third row, its time series in (**d**)). The time series in (**b**), (**c**), and (**d**) originate from the corresponding locations marked with red markers in (**a**). Note that noise was added to each time series, resulting in a temporal signal-to-noise ratio (SNR) of 108. **e, f**: Functional activation maps (*P* < 0.05) of the fitted regressors for pH and BOLD to the Mixture data, respectively. The corresponding regressors are shown below the activation maps. The Mixture ROI is activated in both pH regressor fit (**e**) and BOLD regressor fit (**f**), as it contains both pHi and BOLD effects.

amplifiers–imposed duty cycle limitations, the optimum B_1 and duty cycle were chosen to be 1.5 μT and 32%, respectively. These parameters are close to those for the originally proposed steady-state 3D CEST sequence (41).

The optimized CEST sequence was evaluated in dual BSA/phosphocreatine phantoms (Fig. 2). The strong inverse relationship (R = −0.94, *P* < 0.05) of the normalized signal (S(@3.5 ppm)/S$_0$) with pH (Fig. 2b) suggests that the new CEST sequence is sensitive to pH in the

physiological range, which was further corroborated by ^{31}P pH measurements in the same phantoms (Fig. 2a). The APT-CEST sequence ΔpH sensitivity per acquisition was estimated to be 0.8 using the following formula:

$$\Delta pH_{detectable} = 2 \times sigma \times \frac{\Delta pH}{\Delta S} \qquad [3]$$

where *sigma* is the noise estimate (the average standard deviation across all samples), Δ*pH* (9–5) and Δ*S* (0.955–
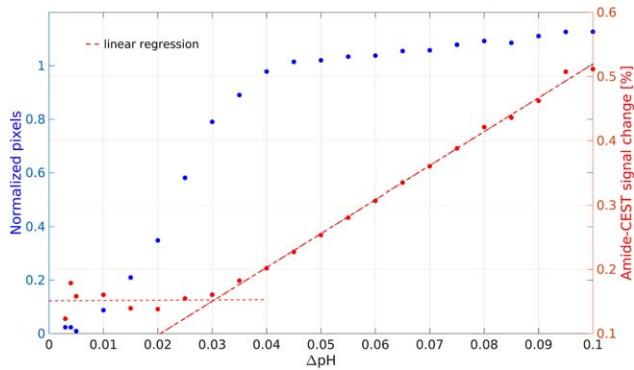
FIG. 7. The APT-CEST (@3.5 ppm) ΔpHi detection limit estimation in the Bloch-McConnell simulated data for the visual paradigm in Figure 5. Normalized pixels (left) axis represents a ratio of activated pixels in the pHFMRI ROI to the number of pixels in the original pHFMRI ROI mask. The ratio deviates from 1 as a result of partial volume effects. The right axis shows a change in isolated amide-CEST signal (%) for each particular ΔpH simulated.

0.940) are the corresponding changes in pH and APT-CEST signal. The ΔpH detectability of APT-CEST sequence was defined as a signal change greater than two standard deviations of the noise distributions (error probability of 5%).

To assess the detection limit of the optimized CEST sequence to pHi changes in vivo, pHi in healthy volunteers was manipulated using short hypercapnic challenges. A BOLD signal increase whose time course resembles that of the PetCO2 trace (Fig. 3a, blue) is evident in both APT-CEST points (pHi sensitive signal at 3.5 ppm) and control points (pH-insensitive signal at 300 ppm) (Fig. 3b). After normalization of the APT-CEST points by the controls, the BOLD signal is no longer evident (Fig. 3c), and the relatively stable level of normalized APT-CEST signal suggests no distinguishable pHi effect. Furthermore, no measureable pHi changes could be detected using ^{31}P MRS in response to two consecutive hypercapnic challenges (Fig. 4). From the literature, the mild hypercapnia stimulus used in this study is
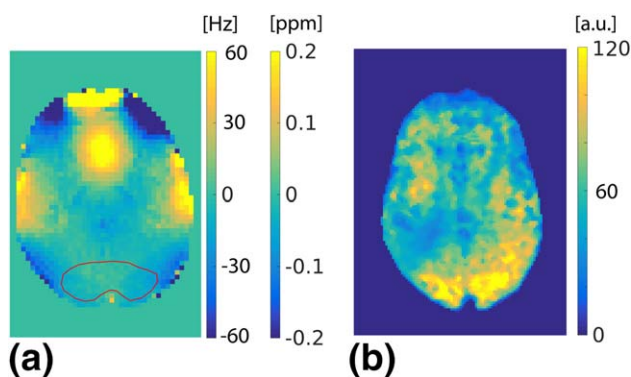

FIG. 8. **a**: Typical B$_0$-field inhomogeneity map optimized using third-order shims. The ROI outlined in red was used to calculate B$_0$-field inhomogeneity across the visual cortex. **b**: Typical temporal signal-to-noise ratio map.

expected to result in a pHi drop of approximately 0.02 ± 0.01 (24). The fact that no pHi changes could be discerned by either APT-CEST or ^{31}P MRS during the hypercapnia stimulus suggests that the limit of detection of ΔpHi by APT-CEST is above 0.02.

The concept of pHi-fMRI (Fig. 5) was tested in the Bloch-McConnell simulations (Fig. 6). To this end, a time series of 2D fMRI dynamic images (Fig. 6a), corresponding to the visual stimulus paradigm in Figure 5, was simulated with the following effects: (i) a combination of BOLD and pHi encoded in "Mixture" region of interest (ROI) (first row, Fig. 6b); (ii) a control for only pHi encoded in "pHFMRI" ROI (second row, Fig. 6c); and (iii) a control for only BOLD encoded in "boldFMRI" (third row, Fig. 6d). A general linear model of three regressors (Fig. 5) was sufficient to separate the effects of pHi and BOLD in the "Mixture" data. In Figure 6e, the pHFMRI ROI shows activation as expected when using the pHi regressor to isolate pHi effects. Similarly, in Figure 6f, the boldFMRI ROI shows activation when using the regressor for BOLD to isolate BOLD effects. Note that the fitted signal changes are much higher for the BOLD effect compared with the pHi effect, indicating a substantial T$_2^*$ weighting for the used APT-CEST sequence. Nonetheless, the BOLD effect can be effectively removed using the RF "off" interleaved dynamic acquisition scheme, allowing isolation of potential pHi signal variations after visual stimulation. In Figures 6e and 6f, the Mixture ROI is also activated, because the underlying signal in this ROI contains both pHi and BOLD effects. The input and output of the model were similar in magnitude within the error introduced by the added noise.

The Bloch-McConnell equations (43) were used to further study the limitations of the model for separating pHi effect from a BOLD contaminated signal. At the experimental temporal SNR, the ΔpHi detection limit of the APT-CEST sequence for the visual stimulus paradigm in Figure 5 was estimated to be 0.03 (Fig. 7). Similarly, the temporal encoding of 100 repetitions in fMRI experiments (Fig. 5) increases the sensitivity by a factor of $\sqrt{100}$; thus, a pH sensitivity of 0.8 (per acquisition point) found in phantoms (Fig. 2) translates to 0.08 for fMRI experiments. These estimates of pH sensitivity obtained from the simulations and phantom experiments explain why no detectable APT-CEST changes were measured during the mild hypercapnia stimulus experiments.

The B$_0$-field inhomogeneity map and the temporal SNR map are show in Figures 8a and 8b, respectively. The inhomogeneity across the visual cortex was calculated to be under 10 Hz, whereas the temporal SNR was found to be 108. The experimental fMRI data of a healthy control is presented in Figure 9. The visual stimulus during the flashing checkboard induced a BOLD effect of approximately 1% in the visual cortex (Fig. 9a). There is some residual activation in the pHi activation map (Fig. 9b); however, no statistically significant pHi effect could be extracted in the visual cortex. These results suggest that pHi changes evoked by the visual stimulus during the flashing checkboard are under 0.03 units pH change.
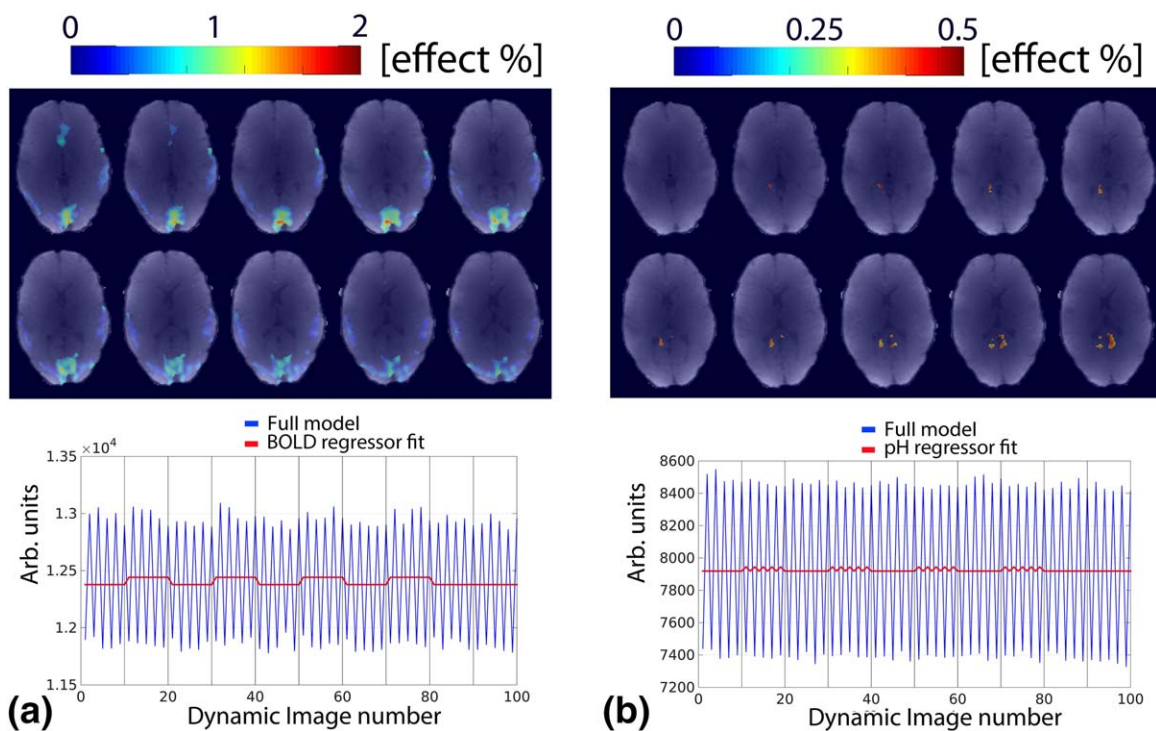
FIG. 9. The BOLD (**a**) and pHi (**b**) functional activation maps ($P < 0.05$) resulting from the visual flashing checkerboard stimulus (top row), along with the corresponding averaged regressors (bottom row). The regressor fit shows the fitted signal variation caused by the effects of pHi and BOLD, respectively. The data shown are that of a single representative subject.

DISCUSSION

The APT-CEST sequence is believed to originate from intracellular compartment (i.e., pHi-weighted contrast). In this work, we present our initial attempts at detecting pHi changes during visual brain activation using APT-CEST at 7 T. To this end, a 3D steady-state pulsed CEST sequence was optimized by means of the Bloch-McConnell simulations in terms of temporal resolution and sensitivity to the pHi-dependent APT-CEST effect. In Bloch-McConnell simulated data, a three-component general linear model was capable of separating the pHi and confounding BOLD effects. In vivo, however, only the BOLD effect could be clearly identified in the visual cortex, and no significant pHi changes could be detected.

The pHi changes in the brain evoked by visual stimuli are expected to be transient; thus, the method to track the related signal variations should have a high temporal resolution. For the steady-state CEST sequence used in this work, there is a trade-off between the steady-state signal and the temporal resolution (Fig. 1a). The highest allowable temporal resolution was determined to be 12.6 s for a signal change within 0.5% of the steady-state signal. To be within RF amplifiers duty cycle limitations, the optimum B_1 amplitude and duty cycle were chosen to be $1.5 \mu T$ and 32%, respectively (Fig. 1b). These optimized parameters are in line with the fact that amide protons are slowly exchanging protons (35) and require a low power level to reach the maximum saturation efficiency (41). The sequence timing (Fig. 1a) and CEST prepulse (Fig. 1b) parameters are largely uncorrelated and can therefore be optimized independently. The

B_0-inhomogeneity correction of CEST data requires acquisition of densely sampled CEST spectra (water saturation shift referencing method) (51), which is not possible when high temporal resolution is desired. To make our CEST sequence relatively insensitive to small B_0-inhomogeneity effects, we chose to use a short CEST prepulse of only 8 ms (267-Hz bandwidth). This also has the advantage of increasing SNR (both image and temporal) by sensitizing the sequence to the whole APT effect (3–4 ppm or 298 Hz at 7 T). The optimized APT-CEST sequence was validated to be pH sensitive in BSA phantoms that are rich in amide protons. The APT-CEST sequence sensitivity to pH changes in BSA phantoms was estimated to be 0.8 (per acquisition point), which translates to 0.08 for fMRI experiments (due to averaging the data from 100 repeated measurements, i.e., $0.8/\sqrt{100}$). Fitting regressors for fMRI data is expected to further increase this pH sensitivity, but the precise estimation is difficult. Although BSA is a good model protein, care has to be taken when directly translating the phantom results to in vivo studies, because of differences in water T_1 relaxation times (52–55), protein concentration, protein conformation, and catalytic microenvironment (56), among others.

The exact magnitude of visual stimuli-evoked pHi changes in the brain is unknown, but it is expected to be relatively small as a result of acid-base homeostasis. Therefore, it is important to estimate the ΔpHi detection limit of the sequence used to detect those changes. From the literature, the short (6 min) mild hypercapnic exposure (Fig. 3a) used in this work is expected to cause a pHi drop of approximately 0.02 ± 0.01 (24). As expected, all points (pHi-sensitive APT-CEST and controls) have

an additional contribution of BOLD effect during the breathing challenge as a result of T_2^* weighting of the echo-planar imaging readout and a finite echo time (Fig. 3b). However, only pHi-sensitive APT-CEST points are expected to be influenced by a pHi effect. This means that normalization of the APT-CEST points by the control data should effectively remove the BOLD contamination, revealing a small ΔpHi effect. As expected, after the normalization, we did not see any BOLD effect. Unfortunately, no visible pHi effect could be discerned either. With these results, we concluded that the ΔpHi detection limit of the APT-CEST scheme is above 0.02. In similar breathing experiments, we tried to detect those pHi changes by using the gold standard (i.e., ^{31}P MRS) (Fig. 4). No pHi changes could be detected even during two consecutive hypercapnic exposures. However, this is not surprising, considering the low pHi precision of ^{31}P MRS itself, which is estimated to be approximately 0.05 (20,57,58). In this work, we chose to do hypercapnic exposures, as those are easy to control. A pHi change of approximately 0.1 with increased lactate detection was reported earlier in hyperventilation experiments (59).

With the knowledge of the optimized sequence parameters and the limitations determined in the previous steps (Figs. 1–4), the APT-CEST sequence was used in the Bloch-McConnell simulations to test the feasibility of pHi-fMRI (Fig. 5). The effects of pHi (0.1 ΔpHi encoded in the pHFMRI ROI in Fig. 6a) and BOLD (1.1% signal change encoded in the boldFMRI ROI in Fig. 6a) were simulated separately and in combination (the Mixture ROI in Fig. 6a), as would be expected in the in vivo fMRI experiments. The simulated time series were corrupted with a Gaussian noise, resulting in a temporal SNR of 108 (matching that of the experimental data). The general linear model was successful in separating the effects of both pH and BOLD from the mixture of two, and the isolated contrast resembles that of the control contrast (the pHFMRI and boldFMRI ROIs were used as controls for pH and BOLD effects in Figs. 6e and 6f, respectively). These results serve as a proof of principle of the feasibility of pHi-fMRI. However, despite the fact that the Bloch-McConnell equations are known to describe chemical exchange processes precisely, it is important to realize that many in vivo parameters used in the simulations are unknown beforehand. As a result, we had to make an assumption on a few parameters, taking the available literature into account. In addition, the magnitude of pHi changes evoked by the neuronal activity in vivo is also unknown, and was assumed in the simulations to be 0.1 (23), which may not correspond with the reality. This level of ΔpHi could be successfully isolated from a strongly BOLD-contaminated MRI signal. The breathing experiments reported in this work appear to be the most practical way to measure the ΔpHi detection limit in the healthy human brain noninvasively. However, those experiments would require extremely high intolerable levels of carbon dioxide to cause a measureable pHi change (Figs. 3 and 4). The advantage of the Bloch-McConnell equations comes from the fact that the influence of many parameters can be studied without actually doing the experiments. By varying the ΔpHi effect, the ΔpHi detection limit of the sequence coupled

with the visual stimulus paradigm was found to be 0.03. This seemingly high pH sensitivity comes from fitting the repetitive temporal pattern of the fMRI experiments with a model with three regressors.

In the in vivo experiments, B_0 inhomogeneity may be an issue, especially for the dynamic measurements used in this study. The B_0 field was optimized across the whole brain using third-order shims (Fig. 8a). Small inhomogeneity (in our case under 10 Hz) in the visual cortex can be neglected, as the CEST prepulse was 8 ms (267 Hz bandwidth), and the APT-CEST effect covers a range of 298 Hz (from 3 to 4 ppm).

The same general linear model, the performance of which was tested in these simulations, was applied to the in vivo fMRI data (Fig. 9) to separate the pHi and BOLD effects evoked by the visual stimulus in healthy human brain. A small BOLD effect (Fig. 9a) of approximately 1% (on average) could be isolated in the visual cortex, but there was no statistically significant pHi effect in the same location (Fig. 9b). The seemingly spurious pHi activation below the ventricles, we attribute to an accidental residual activation, which we observed in a similar location in all three subjects. The fact that a pHi change of 0.1 units could be isolated in the Bloch-McConnell simulations, and the ΔpHi limit of detection for APT-CEST was estimated to be 0.03, suggests that activity-evoked pHi changes in vivo are below 0.03 units. Despite the fact that APT-CEST was unable to detect visual stimuli–evoked pHi changes in this study, it is a powerful tool for quantifying larger pH effects, which has shown potential in identifying ischemic penumbra in multiple studies (36–40).

In this study, we chose a pHi-sensitive APT-CEST technique to detect activity-evoked pHi changes. The results of this study suggest that the pHi changes are extremely small and easily hidden by the larger BOLD effects, which can be mistaken for the desired pHi effects. Thus, care must be taken when interpreting fMRI data using a pHi-sensitive sequence. Therefore, further investigation is required to determine whether the activity-evoked changes in $T_{1\rho}$ contrast, such as reported recently in (23), originated from pH effects or can be attributed to the confounding effects of diffusion (25,27,28), cerebral blood volume (29), inflow (30), and/or BOLD (28).

Limitations

The CEST-MRI of amides, which is sensitive to changes in pH as small as 0.1 (36), has been used in multiple studies to detect the pH-weighted APT effect (36–40). Recently, it has been shown that CEST-MRI of amines may offer higher pH sensitivity compared with APT-CEST (60). However, sufficient labeling of amine protons requires much higher power levels because of their faster exchange rates. The duration of our fMRI experiments was 21 min 14 s, which limited our choice of the pH-sensitive CEST-MRI technique to APT-CEST as a result of RF amplifiers limitations. Because of a low B_1, no fast exchanging protons have been included in the simulations. The currently available B_1 correction methods (61,62) would have increased the scan time dramatically,

and therefore have not been used. Although there could be a spatial B_1 pattern, its temporal pattern remains unchanged. Even though both BOLD (63) and pH (phantom data not shown) can influence water T_1, their effects are negligibly small and have not been included in the model. The exchange rate was assumed to be only a function of pH (35).

CONCLUSIONS

In this report, we present our initial attempts at detecting neuronal activity-evoked pH changes by APT-CEST MRI at 7 T. In theory, it was successfully shown that as small as 0.03 units pH change can be separated from a 1.1% BOLD effect at the experimentally determined temporal SNR of 108. During the visual stimuli experiments in vivo, however, only the BOLD effect could be detected in the visual cortex with no significant pH changes. The results of this study suggest that neuronal activity-evoked pH changes are under 0.03, which is extremely difficult to detect using the existing techniques.

REFERENCES

1. Boxerman JL, Bandettini PA, Kwong KK, Baker JR, Davis TL, Rosen BR, Weisskoff RM. The intravascular contribution to fMRI signal change: Monte Carlo modeling and diffusion-weighted studies in vivo. Magn Reson Med 1995;34:4–10.
2. Buxton RB, Frank LR. A model for the coupling between cerebral blood flow and oxygen metabolism during neural stimulation. J Cereb Blood Flow Metab 1997;17:64–72.
3. Ogawa S, Menon RS, Kim SG, Ugurbil K. On the characteristics of functional magnetic resonance imaging of the brain. Annu Rev Biophys Biomol Struct 1998;27:447–474.
4. D'Esposito M, Deouell LY, Gazzaley A. Alterations in the BOLD fMRI signal with ageing and disease: a challenge for neuroimaging. Nat Rev Neurosci 2003;4:863–872.
5. Iannetti GD, Wise RG. BOLD functional MRI in disease and pharmacological studies: room for improvement? Magn Reson Imaging 2007;25:978–988.
6. Chesler M, Kaila K. Modulation of pH by neuronal activity. Trends Neurosci 1992;15:396–402.
7. Meyer TM, Munsch T, Pape HC. Activity-related changes in intracellular pH in rat thalamic relay neurons. Neuroreport 2000;11:33–37.
8. Deitmer JW, Rose CR. pH regulation and proton signalling by glial cells. Prog Neurobiol 1996;48:73–103.
9. Chesler M. The regulation and modulation of pH in the nervous system. Prog Neurobiol 1990;34:401-427.
10. Siesjo BK. Acid-base homeostasis in the brain: physiology, chemistry, and neurochemical pathology. In: Kogure K, Hossmann, KA, Siesjo BK, Welsh FA, editors. Progress in brain research. Oxford, United Kingdom: Elsevier; 1985. pp 121–154.
11. Kaila K, Voipio J. Postsynaptic fall in intracellular pH induced by GABA-activated bicarbonate conductance. Nature 1987;330:163–165.
12. Chesler M, Chan CY. Stimulus-induced extracellular pH transients in the in vitro turtle cerebellum. Neuroscience 1988;27:941–948.
13. Kaila K, Saarikoski J, Voipio J. Mechanism of action of GABA on intracellular pH and on surface pH in crayfish muscle fibres. J Physiol 1990;427:241–260.
14. Chen, JCT, Chesler M. Modulation of extracellular pH by glutamate and GABA in rat hippocampal slices. J Neurophysiol 1992;68:342–344.
15. Moody WJ. Effects of intracellular H + on the electrical properties of excitable cells. Annu Rev Neurosci 1984;7:257–278.
16. Ng TC, Majors AW, Vijayakumar S, et al. Human neoplasm pH and response to radiation therapy: P-31 MR spectroscopy studies in situ. Radiology 1989;170:875–878.
17. Petroff OAC, Prichard JW, Behar KL, Alger JR, den Hollander JA, Shulman RG. Cerebral intracellular pH by 31P nuclear magnetic resonance spectroscopy. Neurology 1985;35:781–788.
18. Moon RB, Richards JH. Determination of intracellular pH by 31P magnetic resonance. J Biol Chem 1973;248:7276–7278.
19. Soto GE, Zhu Z, Evelhoch JL, Ackerman JJ. Tumor 31P NMR pH measurements in vivo: a comparison of inorganic phosphate and intracellular 2-Deoxyglucose-6-Phosphate as pHnmr indicators in murine radiation-induced fibrosarcoma-1. Magn Reson Med 1996;36:698–704.
20. Khlebnikov V, Wijnen J, Wybe JM, Klomp DWJ. 31P MRSI studies in patients with cancer. In: Webb GA, editor. Annual reports on NMR spectroscopy. Oxford, United Kingdom: Academic Press; 2016, pp 319–368.
21. Jin T, Autio J, Obata T, Kim SG. Spin-locking versus chemical exchange saturation transfer MRI for investigating chemical exchange process between water and labile metabolite protons. Magn Reson Imaging 2011;65:1448–1460.
22. van Zijl PCM, Yadav NN. Chemical exchange saturation transfer (CEST): What is in a name and what isn't? Magn Reson Med 2011;65:927–948.
23. Magnotta VA, Heo HY, Dlouhy BJ, Dahdaleh NS, Follmer RL, Thedens DR, Welsh MJ, Wemmie JA. Detecting activity-evoked pH changes in human brain. Proc Natl Acad Sci USA 2012;109:8270–8273.
24. Duvvuri U, Goldberg AD, Kranz JK, Hoang L, Reddy R, Wehrli FW, Wand AJ, Englander SW, Leigh JS. Water magnetic relaxation dispersion in biological systems: the contribution of proton exchange and implications for the noninvasive detection of cartilage degradation. Proc Natl Acad Sci USA 2001;98:12479–12484.
25. Kettunen MI, Gröhn OH, Silvennoinen MJ, Penttonen M, Kauppinen RA. Effects of intracellular pH, blood, and tissue oxygen tension on T1ρ relaxation in rat brain. Magn Reson Med 2002;48:470–477.
26. Engelhardt RT, Johnson GA. T1 rho relaxation and its application to MR histology. Magn Reson Med 1996;35:781–786.
27. Spear JT, Zu Z, Gore JC. Dispersion of relaxation rates in the rotating frame under the action of spin-locking pulses and diffusion in inhomogeneous magnetic fields. Magn Reson Med 2014;71:1906–1911.
28. Rane S, Spear JT, Zu Z, Donahue MJ, Gore JC. Functional MRI using spin lock editing preparation pulses. Magn Reson Imaging 2014;32:813–818.
29. Hulvershorn J, Borthakur A, Bloy L, Gualtieri EE, Reddy R, Leigh JS, Elliott MA. T1ρ contrast in functional magnetic resonance imaging. Magn Reson Med 2005;54:1155–1162.
30. Deng M, Zhao F, Yuan J, Ahuja AT, Wan Y-XJ. Liver T1ρ MRI measurement in healthy human subjects at 3 T: a preliminary study with a two-dimensional fast-field echo sequence. Br J Radiol 2012;85:e590–e595.
31. Liepinsh E, Otting G. Proton exchange rates from amino acid side chains–implications for image contrast. Magn Reson Med 1996;35:30–42.
32. Zhou J, Lal B, Wilson DA, Laterra J, van Zijl PC. Amide proton transfer (APT) contrast for imaging of brain tumors. Magn Reson Med 2003;50:1120–1126.
33. Jones CK, Schlosser MJ, van Zijl PC, Pomper MG, Golay X, Zhou J. Amide proton transfer imaging of human brain tumors at 3T. Magn Reson Med 2006;56:585–592.
34. Wen Z, Hu S, Huang F, Wang X, Guo L, Quan X, Wang S, Zhou J. MR imaging of high-grade brain tumors using endogenous protein and peptide-based contrast. NeuroImage 2010;51:616–622.
35. Zhou J, Payen JF, Wilson DA, Traystman RJ, van Zijl PC. Using the amide proton signals of intracellular proteins and peptides to detect pH effects in MRI. Nature Med 2003;9:1085–1090.
36. Tee YK, Harston GW, Blockley N, et al. Comparing different analysis methods for quantifying the MRI amide proton transfer (APT) effect in hyperacute stroke patients. NMR Biomed 2014;27:1019–1029.
37. Zhou J, Sun W, Huang J, van Zijl PC. Detection of the ischemic penumbra using pH-weighted MRI. J Cereb Blood Flow Metab 2007;27:1129–1136.
38. Zhou J, van Zijl P. Defining an acidosis-based ischemic penumbra from pH-weighted MRI. Transl Stroke Res 2011;3:76–83.
39. Tietze A, Blicher J, Mikkelsen IK, Østergaard L, Strother MK, Smith SA, Donahue MJ. Assessment of ischemic penumbra in patients with hyperacute stroke using amide proton transfer (APT) chemical exchange saturation transfer (CEST) MRI. NMR Biomed 2014;27:163–174.

40. Harston GW, Tee YK, Blockley N, et al. Identifying the ischaemic penumbra using pH-weighted magnetic resonance imaging. Brain 2015;138:36–42.

41. Jones CK, Polders D, Hua J, Zhu H, Hoogduin HJ, Zhou J, Luijten P, van Zijl PC. In vivo three-dimensional whole-brain pulsed steady-state chemical exchange saturation transfer at 7T. Magn Reson Med 2012;67:1579–1589.

42. McConnell HM. Reaction rates by nuclear magnetic resonance. J Chem Phys 1958;28:430–431.

43. Woessner DE, Zhang S, Merritt ME, Sherry AD. Numerical solution of the Bloch equations provides insights into the optimum design of PARACEST agents for MRI. Magn Reson Med 2005;53:790–799.

44. Mougin O, Clemence M, Peters A, Pitiot A, Gowland P. High-resolution imaging of magnetisation transfer and nuclear Overhauser effect in the human visual cortex at 7 T. NMR Biomed 2013;26:1508–1517.

45. Ramani A, Dalton C, Miller DH, Tofts PS, Barker GJ. Precise estimate of fundamental in-vivo MT parameters in human brain in clinically feasible times. JMRI 2002;20:721–731.

46. Ackerman JJ, Soto GE, Spees WM, Zhu Z, Evelhoch JL. The NMR chemical shift pH measurement revisited: analysis of error and modeling of a pH dependent reference. Magn Reson Med 1996;36:674–683.

47. Jenkinson M, Smith S. A global optimisation method for robust affine registration of brain images. Med Image Anal 2001;5:143–156.

48. Jenkinson M, Bannister P, Brady M, Smith S. Improved optimization for the robust and accurate linear registration and motion correction of brain images. NeuroImage 2002;17:825–841.

49. Wright PJ, Mougin OE, Totman JJ, et al. Water proton T1 measurements in brain tissue at 7, 3, and 1.5T using IR-EPI, IR-TSE, and MPRAGE: results and optimization. Magma 2008;21:121–130.

50. Rooney WD, Johnson G, Li X, Cohen ER, Kim SG, Ugurbil K, Springer CS Jr. Magnetic field and tissue dependencies of human brain longitudinal 1H2O relaxation in vivo. Magn Reson Med 2007;57:308–318.

51. Kim M, Gillen J, Landman BA, Zhou J, van Zijl PC. Water saturation shift referencing (WASSR) for chemical exchange saturation transfer (CEST) experiments. Magn Reson Med 2009;61:1441–1450.

52. Zaiss M, Xu J, Goerke S, Khan IS, Singer RJ, Gore JC, Gochberg DF, Bachert P. Inverse Z-spectrum analysis for spillover-, MT-, and T1-corrected steady-state pulsed CEST-MRI—application to pH-weighted MRI of acute stroke. NMR Biomed 2014;27:240–252.

53. Zaiss M, Windschuh J, Paech D, et al. Relaxation-compensated CEST-MRI of the human brain at 7T: unbiased insight into NOE and amide signal changes in human glioblastoma. NeuroImage 2015;112:180–188.

54. Khlebnikov V, Polders D, Hendrikse J, Robe PA, Voormolen EH, Luijten PR, Klomp DW, Hoogduin H. Amide proton transfer (APT) imaging of brain tumors at 7 T: the role of tissue water T1-relaxation properties. Magn Reson Med 2017;77:1525–1532.

55. Khlebnikov V, Siero JC, Wijnen J, Visser F, Luijten PR, Klomp DW, Hoogduin H. Is there any difference in amide and NOE CEST effects between white and gray matter at 7T? J Magn Reson 2016;272:82–86.

56. Liepinsh E, Otting G. Proton exchange rates from amino acid side chains—implications for image contrast. Magn Reson Med 1996;35:30–42.

57. Roberts JK, Wade-Jardetzky N, Jardetzky O. Intracellular pH measurements by 31P nuclear magnetic resonance. Influence of factors other than pH on 31P chemical shifts. Biochemistry 1981;20:5389–5394.

58. Ackerman JJH, Soto GE, Spees WM, Zhu Z, Evelhoch JL. The NMR chemical shift pH measurement revisited: analysis of error and modeling of a pH dependent reference. Magn Reson Med 1996;36:674–683.

59. van Rijen PC, Luyten PR, van der Sprenkel JW, Kraaier V, van Huffelen AC, Tulleken CA, den Hollander JA. 1H and 31P NMR measurement of cerebral lactate, high-energy phosphate levels, and pH in humans during voluntary hyperventilation: associated EEG, capnographic, and Doppler findings. Magn Reson Med 1989;10:182–193.

60. Zaiss, M, Windschuh, J, Goerke, S, et al. Downfield-NOE-suppressed amide-CEST-MRI at 7 Tesla provides a unique contrast in human glioblastoma. Magn Reson Med 2017;77:196–208.

61. Windschuh J, Zaiss M, Meissner JEE, et al. Correction of B1-inhomogeneities for relaxation-compensated CEST imaging at 7 T. NMR Biomed 2015;28:529–537.

62. Khlebnikov V, Windschuh J, Siero JCW, Zaiss M, Luijten PR, Klomp DWJ, Hoogduin H. On the transmit field inhomogeneity correction of relaxation-compensated amide and NOE CEST effects at 7T. NMR Biomed 2017;30.

63. Janick PA, Hackney DB, Grossman RI, Asakura T. MR imaging of various oxidation states of intracellular and extracellular hemoglobin. Am J Neuroradiol 1991;12:891–897.